Peer-reviewed version available at *Energies* **2018**, *11*, 2458; doi:10.3390/en11092458

Article

THD reduction in Wind Energy System using Type-4 Wind Turbine/PMSG applying the Active Front-End Converter Parallel Operation

Nadia Maria Salgado-Herrera [1,*], David Campos-Gaona[1], Olimpo Anaya-Lara[1], Aurelio Medina-Rios[2], Roberto Tapia-Sanchez[2] and Juan Ramon Rodriguez-Rodriguez[3,]

[1] Institute for Energy and Environment, University of Strathclyde, Glasgow, G1 1XW, UK; nadia.salgado-herrera@strath.ac.uk, d.campos-gaona@strath.ac.uk, olimpo.anaya-lara@eee.strath.ac.uk

[2] Facultad de Ingenieria Electrica, División de estudios de posgrado, Universidad Michoacana de San Nicolas de Hidalgo, Morelia, Michoacan, CP 58030, México; amedinr@gmail.com, rtsanchez@dep.fie.umich.mx

[3] Universidad Nacional Autónoma de México; Facultad de Ingeniería; Departamento de Energía Eléctrica. Coyoacán, Ciudad de México; Jr_rodriguez@fi-b.unam.mx

* Correspondence: nadia.salgado-herrera@strath.ac.uk; Tel.: +5214431019237

Abstract: In this paper, the active front-end (AFE) converter topology for the total harmonic distortion (THD) reduction in a wind energy system (WES) is used. A higher THD results in serious pulsations in the wind turbine (WT) output power and in several power losses at the WES. The AFE converter topology improves capability, efficiency and reliability in the energy conversion devices; by modifying a conventional back-to-back converter, from using a single voltage source converter (VSC) to use *p*VSC connected in parallel the AFE converter is generated. The THD reduction is done by applying a different phase shift angle at the carrier of digital sinusoidal pulse width modulation (DSPWM) switching signals of each VSC. To verify the functionality of the proposed methodology, the WES simulation in Matlab-Simulink® is analyzed, and the experimental laboratory tests using the concept of rapid control prototyping and the real-time simulator Opal-RT Technologies© is achieved. The obtained results show a type-4 WT with total output power of 6MVA, generating a THD reduction up to 5.5 times at the WES.

Keywords: Active Front-End converter; back-to-back converter; PMSG; THD; Type-4 wind turbine; wind energy system; Opal-RT Technologies©

1. Introduction

Nowadays, the wind energy systems (WES) have increased dramatically, as evidenced of this; in 2013, WES were installed in more than 80 countries, generating a power of 240 GW [1], in 2014, the generation reached a capacity of 369.9 GW [2], in 2015, a production of 432.883 GW is generated [3], by the end of 2016 a global generation of 487 GW is installed [4] and in 2021 the installed capacity is expected to exceed 800 GW [5]. Within the types of variable speed wind turbines (WT) there are three types: type-2 (squirrel-cage induction generator (SCIG)), type-3 (double fed induction generator (DFIG)) and type-4 (squirrel-cage induction generator (SCIG)/permanent magnet synchronous generator (PMSG) with full scale back-to-back converter); in which, the type-2 has a 10% of variability in the rotor, the type-3 has a 30% of variability and the type-4 has a 60% of the variability of the rotor speed [6]. The type-3 (DFIG) wind turbine schemes constitute the majority of variable speed commerce applications; however, the type-4 WT with a PMSG (WT-PMSG) is an attractive and the best option since this is not directly connected to the grid, presenting advantages

Preprints (www.preprints.org) | NOT PEER-REVIEWED | Posted: 4 September 2018 doi:10.20944/preprints201809.0054.v1

Peer-reviewed version available at Energies 2018, 11, 2458; doi:10.3390/en11092458

such as: high efficiency, increased reliability, major variable speed operation and low cost in maintenance and installation, due the absence of gearboxes [7].

Then, in the type-4 WT-PMSG installation the important aspects to prevent are associated problems with the wind nature fluctuations. For example: the flicker generation is mainly caused by load flow changes, due to its continuous operation [8]; a power factor not unity, this characteristic happens due the modulation index of the back-to-back converter is not high [9]. Voltage sags occur by the sudden changes in the rotor speed of the type-4 WT-PMSG and cause a decrement in the transferred power from the dc-link to the grid [10]; and a higher THD is mainly produced by the power converters switching, this results in serious pulsations in the type-4 WT-PMSG output power and in several power losses at the WES [11-12]. All these problems can be mitigate through the full-scale back-to-back converter in the type-4 WT-PMSG scheme, and this generate the next advantages [13-16]: *i)* Bidirectional power flow; *ii)* Adjustable dc-link voltage; *iii)* A sinusoidal grid-side current with exchange of active and reactive power. These advantages are possible because the total generated power by the type-4 WT-PMSG on the AC grid is supplied through the back-to-back converter.

However, its implementation is very difficult, since this must handle very high powers up to 6MVA. The Active Front-End (AFE) converter topology improves the capability, efficiency and reliability in the energy conversion devices connected to the WES; this is generated by modifying a conventional back-to-back converter, from using a single voltage source converter (VSC) to use *p*VCS connected in parallel, as shown in Figure 1. Through the AFE converter parallel topology is possible the follow advantages: *i)* Increase the converter power capacity; *ii)* Minimized size of each VSC unit, which manages a portion of the total nominal power; *iii)* A reduced ripple on the injected current, which improves the voltages quality at the Point of Common Coupling (PCC); *iv)* An increased equivalent switching frequency, generating a smaller passive filter on AC-side and the reduction of switching losses brings a lower THD.

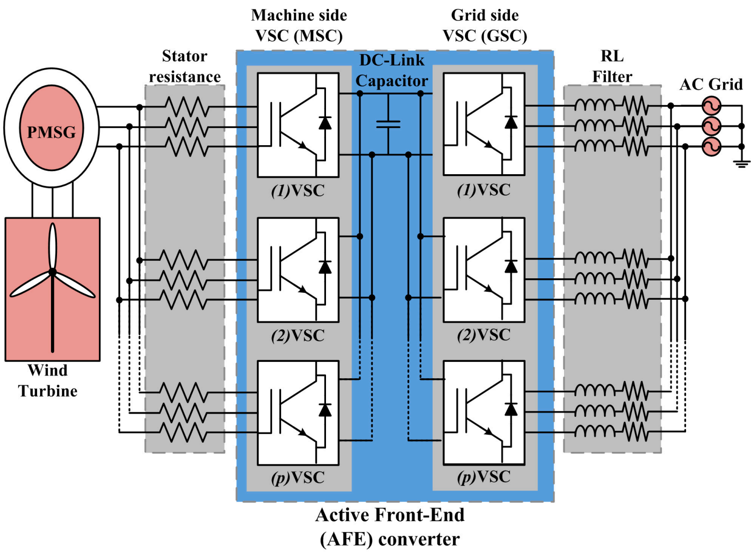

Figure 1. Type-4 WT connected at WES through the AFE converter parallel topology

As evidence, in [3] the authors describe the principal WT manufacturers, these in low voltage (LV) and medium voltage (MV) technologies are classified, generating powers ratings of >3MVA and <3MVA, respectively. In the open literature exists some research works that address the AFE converter topology applied to WES; for example, in [17] the authors present analytically and experimentally the control method for the current balance in an AFE power converter of 600kVA, this is a very important topic in the parallel connection of power converters, however, the authors make the AFE converter analysis connecting only two VSCs in parallel, generating: a THD of 4.32% (three times higher than in our research work with THD of 1.23%); in addition, they use the space

Preprints (www.preprints.org) | NOT PEER-REVIEWED | Posted: 4 September 2018 doi:10.20944/preprints201809.0054.v1

Peer-reviewed version available at *Energies* **2018**, *11*, 2458; doi:10.3390/en11092458

vector modulation for the switching of VSCs, which it generates a more complex control if *p*VSC in parallel are connected.

The AFE converter topology for the THD reduction in WES is made. To verify the functionality and robustness of the proposed methodology, an AFE converter formed with three VSCs connected in parallel at the WES is incorporated. The WES simulation in Matlab-Simulink® is analyzed, and the experimental laboratory tests using the concept of rapid control prototyping and the real-time simulator Opal-RT\ is achieved. The obtained results show a WES prototyping that incorporates a type-4 wind turbine with total output power of 6MVA and a THD reduction up to 5.5 times

2. Modeling of the Type-4 WT-PMSG

The AFE converter structure consists in two power electronics converters: a machine side VSC (MSC) to provide power conversion between medium ac voltage and low DC voltage levels, and a grid side VSC (GSC) to generate the voltages required by the consumers [18], for which, the next sections describe the control modeling of MSC and GSC and these in Figure 2 are shown.

2.1. Modeling of the machine side VSC control at AFE converter

The MSC provides the rotor flux frequency control, thus enabling the rotor shaft frequency to optimally track wind speed [19]. The time-domain relationship of the VSC AC-side is given by:

$$\left[d\left(i_{MSC}^{h}\left(t\right)\right)/dt\right]=-\left(R_{MSC}^{h}/L_{MSC}^{h}\right)\left[i_{MSC}^{h}(t)\right]+\left(1/L_{MSC}^{h}\right)\left[v_{MSC}^{h}\left(t\right)\right]-\left(1/L_{MSC}^{h}\right)\left[v_{WT-PMSG}^{h}\left(t\right)\right] \tag{1}$$

where h is the MSC three-phase vector (a,b,c), L_{MSC} is the PMSG armature inductance, R_{MSC} is the PMSG stator phase resistance, v_{MSC} and i_{MSC} are the MSC voltage and current, respectively, $v_{WT\text{-}PMSG}$ is the generated WT-PMSG voltage.

Then, the dq reference frame model derived from the AC-side of the MSC, including the inductances cross coupling, is described as:

$$\left[\frac{d(i_{MSC}^{d}(t))}{dt}\right]=-\left(\frac{R_{MSC}^{d}}{L_{MSC}^{d}}\right)\left[i_{MSC}^{d}\left(t\right)\right]+\left(\frac{\omega_{rPMSG}L_{MSC}^{q}}{L_{MSC}^{d}}\right)\left[i_{MSC}^{q}\left(t\right)\right]+\left[\frac{v_{MSC}^{d}(t)}{L_{MSC}^{d}}\right]-\left[\frac{v_{WT-PMSG}^{d}(t)}{L_{MSC}^{d}}\right] \tag{2a}$$

$$\left[\frac{d(i_{MSC}^{q}(t))}{dt}\right]=-\left(\frac{R_{MSC}^{q}}{L_{MSC}^{q}}\right)\left[i_{MSC}^{q}(t)\right]-\left(\frac{\omega_{rPMSG}L_{MSC}^{d}}{L_{MSC}^{q}}\right)\left[i_{MSC}^{d}(t)\right]-\left[\frac{(\lambda_{mPMSG})(\omega_{rPMSG})}{L_{MSC}^{q}}\right]+\left[\frac{v_{MSC}^{q}(t)}{L_{MSC}^{q}}\right]-\left[\frac{v_{WT-PMSG}^{q}(t)}{L_{MSC}^{q}}\right] \tag{2b}$$

where ω_{rPMSG} is the PMSG rotor angular velocity; λ_{mPMSG} is the maximum flux linkage generated by the PMSG rotor magnets and transferred to the stator windings.

The generated MSC voltage is given by:

$$\left[v_{MSC}^{g}(t)\right]=\left(1/2\right)\left[m_{MSC}^{g}(t)*V_{DC}(t)\right] \tag{3}$$

where g is the dq components reference frame vector of the MSC, VDC is the DC-link voltage, m_{MSC}^{g} is the modulated index vector.

Making $L_{MSC}=L_{MSC}^{d}=L_{MSC}^{q}$, the presence of $\omega_{rPMSG}L_{MSC}$ in (2) indicates the coupled dynamics between i_{MSC}^{d} and i_{MSC}^{q}. To decouple these dynamics, the m_{MSC}^{g} vector signals are changed, based in the dq reference frame, i.e.

$$\left[m_{MSC}^{d}(t)\right]=\left(2/V_{DC}(t)\right)\left[\mathrm{E}_{MSC}^{d}(t)-\left(\left(\omega_{rPMSG}\cdot L_{MSC}\right)i_{MSC}^{q}(t)\right)+v_{WT-PMSG}^{d}(t)\right] \tag{4a}$$

$$\left[m_{MSC}^{q}(t)\right]=\left(2/V_{DC}(t)\right)\left[\mathrm{E}_{MSC}^{q}(t)+\left(\left(\omega_{rPMSG}\cdot L_{MSC}\right)i_{MSC}^{d}(t)\right)+\lambda_{mPMSG}\omega_{rPMSG}+v_{WT-PMSG}^{q}(t)\right] \tag{4b}$$

where $E_{MSC}^{d}(t)$ and $E_{MSC}^{q}(t)$ are two additional control inputs.

The MSC plant is obtained by substituting (4) into (3), subsequently, (3) is replacing into (2) generating a first order lineal system that, in Equation (5) is described.

$$\left[\mathrm{E}_{MSC}^{g}(t)\right]=L_{MSC}\left[di_{MSC}^{g}(t)/dt\right]+R_{MSC}\left[i_{MSC}^{g}(t)\right] \tag{5}$$

Equation (5) in the time domain is represented; its representation in the frequency domain is shown in (6); which describe a decoupled and first-order linear system, controlled through $E_{MSC}^{g}(s)$.

$$\left[\mathrm{E}_{MSC}^{g}(s)\right]=\left(sL_{MSC}+R_{MSC}\right)\left[i_{MSC}^{g}(s)\right] \tag{6}$$

Preprints (www.preprints.org) | NOT PEER-REVIEWED | Posted: 4 September 2018 doi:10.20944/preprints201809.0054.v1

Peer-reviewed version available at *Energies* **2018**, *11*, 2458; doi:10.3390/en11092458

Rewriting equation (6), the transfer function representing the MSC plant is given, i.e.

$$\left[i^{g}_{MSC}(s)\right]=\left[E^{g}_{MSC}(s)\right]\left(sL_{MSC}+R_{MSC}\right)^{-1} \tag{7}$$

With the purpose of tracking the $i^{g}_{MSC}(s)$ reference commands in the loop, the proportional-integral (PI) compensators are used, obtaining:

$$\left[E^{g}_{MSC}(s)\right]\approx\left[k^{g}_{MSC}(s)\right]=\left[\frac{(\alpha_{MSC}skp^{g}_{MSC}+\alpha_{MSC}ki^{g}_{MSC})}{\alpha_{MSC}s}\right]=\left[\left(\frac{\alpha_{MSC}}{s}\right)\left(\frac{(skp^{g}_{MSC}+ki^{g}_{MSC})}{\alpha_{MSC}}\right)\right] \tag{8}$$

where kp^{g}_{MSC} and ki^{g}_{MSC} are the proportional and integral gains, respectively, $\alpha_{MSC}=2.2/\tau_{MSC}$ and τ_{MSC} is compensator response time.

Substituting Equation (8) into (7), the closed loop transfer function $\left[\iota^{g}_{MSC}(s)\right]$ is formed:

$$\left[\iota^{g}_{MSC}(s)\right]\approx\left[i^{gref}_{MSC}(s)-i^{g}_{MSC}(s)\right]=\left[\left(\frac{\alpha_{MSC}}{s}\right)\left(\frac{skp^{g}_{MSC}(s)+ki^{g}_{MSC}(s)}{\alpha_{MSC}}\right)\left(\frac{1}{sL_{MSC}(s)+R_{MSC}(s)}\right)\right] \tag{9}$$

If in open loop the expression (9) tends to be ∞ when $s=j\omega\rightarrow 0$, this guarantees that, in closed loop the system will not have a phase sift delay.

Based on (9), the relation between the plant pole and the PI compensator zero is obtained through (10), generating the kp^{g}_{MSC} and ki^{g}_{MSC} control gains.

$$\left[kp^{g}_{MSC}\right]=\left[\alpha_{MSC}L_{MSC}\right]=\left[\left(2.2/\tau_{MSC}\right)L_{MSC}\right] \tag{10a}$$

$$\left[ki^{g}_{MSC}\right]=\left[\alpha_{MSC}R_{MSC}\right]=\left[\left(2.2/\tau_{MSC}\right)R_{MSC}\right] \tag{10b}$$

Compensator response time, τ_{MSC}, in the range from 5ms to 0.5ms is selected, in this case a τ_{MSC}=2.2ms is designated.

2.2. Modeling Power transfer control between the WT-PMSG and AFE converter

In the WT-PMSG power transfer modeling are considered the next power-speed characteristics [20]: *i)* the base angular velocity of the WT is determined by the base rotor angular velocity of the PMSG, $\omega_{WTb}=\omega_{rPMSGb}$; *ii)* The WES base power is determined by the WT-PMSG nominal power, $P_{WESb}=P_{WT\text{-}PMSGb}$; *iii)* The output base power of the AFE converter is determined by the base WES power, $P_{AFEb}=P_{WESb}$; this power is transferred from WT to PMSG through the electric torque, this is represented by:

$$\left[T_{ePMSG}\right]=\left(3/2\right)\left[\left((L^{d}_{MSC}-L^{q}_{MSC})i^{d}_{MSC}i^{q}_{MSC}\right)+(\lambda_{mPMSG}i^{q}_{MSC})\right] \tag{11}$$

where T_{ePMSG} is the PMSG electrical torque, L^{d}_{MSC} and L^{q}_{MSC} are the *dq* reference frame components of the PMSG armature inductance.

However, considering that the rotor has a cylindrical geometry, then it is established that, $L^{d}_{MSC}=L^{q}_{MSC}$ [21], generating (12).

$$\left[T_{ePMSG}\right]=\left((3/2)\lambda_{mPMSG}\right)\left[i^{q}_{MSC}\right] \tag{12}$$

Then, to realize the WT-PMSG variable speed control it is necessary to generate the plant model that represents it. Therefore, in (13) the dynamic characteristics are shown as a time function that it represents:

$$\left[\frac{d(\omega_{rPMSG})}{dt}\right]=\frac{1}{2H}\left[T_{mWT}-T_{ePMSG}-D\omega_{rPMSG}(t)\right] \tag{13}$$

where D is the PMSG viscous damping, H is the inertia constant (s), T_{mWT} is the WT mechanical torque.

Equation (13) analyzes the WT-PMSG in the time domain; however, the WT-PMSG plant representation requires a transfer function to design the ω_{rPMSG} control. By using Laplace transformation, the WT-PMSG plant in the frequency domain is represented, i.e.:

$$\left[\omega_{rPMSG}(s)\right]=\left[\left(T_{mWT}-T_{ePMSG}\right)\left(2Hs+D\right)^{-1}\right] \tag{14}$$

Preprints (www.preprints.org) | NOT PEER-REVIEWED | Posted: 4 September 2018 doi:10.20944/preprints201809.0054.v1

Peer-reviewed version available at *Energies* **2018**, *11*, 2458; doi:10.3390/en11092458

Equation (14) shows a multiple inputs single output system (MISO); however, due in steady state it is fulfilled that $T_{mWT} \approx T_{ePMSG}$, then, in the control design is considered that $T_{mWT} = 0$; generating a single input single output system (SISO), as shown in (15).

$$\left[\frac{\omega_{rPMSG}(s)}{-T_{ePMSG}}\right] = \left[\frac{1}{2Hs+D}\right] \tag{15}$$

With the purpose of tracking the ω_{PMSG} reference commands in the close loop transfer function, the proportional-integral (PI) compensators are used, obtaining:

The feedback loop $\left[\iota^{q}_{rPMSG}(s)\right]$ is:

$$\left[\iota^{q}_{rPMSG}(s)\right] = \left[\omega^{ref}_{rPMSG}(s) - \omega_{rPMSG}(s)\right] = \left[\left(\frac{\alpha_{PMSG}}{s}\right)\left(\frac{(skp^{q}_{rPMSG} + ki^{q}_{rPMSG})}{\alpha_{PMSG}}\right)\left(\frac{1}{(2Hs+D)}\right)\right] \tag{16}$$

where kp^{q}_{rPMSG} and ki^{q}_{rPMSG} are the proportional and integral gains, respectively.

From (16), the relation between the plant pole and PI compensator zero is obtained and the control gains using the next expression are generated:

$$\left[kp^{q}_{rPMSG}\right] = \left[2H\alpha_{PMSG}\right] = \left[\left(2.2/\tau_{PMSG}\right)2H\right] \tag{17a}$$

$$\left[ki^{q}_{rPMSG}\right] = \left[\alpha_{PMSG}D\right] = \left[\left(2.2/\tau_{PMSG}\right)D\right] \tag{17b}$$

where the subscript τ_{PMSG} is the response time by the closed loop of the WT-PMSG first order transfer function. This is selected according to the WT-PMSG transferred power and this must be at least ten times higher than τ_{MSC}.

2.3. Modeling of the grid side VSC control of the AFE converter

The GSC is used to keep the DC-link constant, transferring the generated power between the WT-PMSG and AC grid. The time-domain relationship of the VSC AC-side is given by:

$$\left[d\left(i^{l}_{GSC}(t)\right)/dt\right] = -\left(R^{l}_{GSC}/L^{l}_{GSC}\right)\left[i^{l}_{GSC}(t)\right] + \left(1/L^{l}_{GSC}\right)\left[v^{l}_{GSC}(t)\right] - \left(1/L^{l}_{GSC}\right)\left[v^{l}_{WES}(t)\right] \tag{18}$$

where l is the VSC three-phase vector (a,b,c), L_{GSC} and R_{GSC} are the RL filter parameters through which the AFE converter is connected to the grid, v_{GSC} and i_{GSC} are the GSC voltage and current, respectively; v_{WES} is the generated WES voltage.

Then, from (18) the derived dq model is described as:

$$L_{GSC}\left(di^{d}_{GSC}(t)/dt\right) = \left(\omega_{0}\cdot L_{GSC}\right)\left[i^{q}_{GSC}(t)\right] - \left(R_{GSC}\right)\left[i^{d}_{GSC}(t)\right] + \left[v^{d}_{GSC}(t)\right] - \left[v^{d}_{WES}(t)\right] \tag{19a}$$

$$L_{GSC}\left(di^{q}_{GSC}/dt\right) = -\left(\omega_{0}\cdot L_{GSC}\right)\left[i^{d}_{GSC}(t)\right] - \left(R_{GSC}\right)\left[i^{q}_{GSC}(t)\right] + \left[v^{q}_{GSC}(t)\right] - \left[v^{q}_{WES}(t)\right] \tag{19b}$$

where ω_0 is the WES angular frequency; the generated GSC voltages are given by:

$$v^{k}_{GSC}(t) = \left(V_{DC}/2\right)\left[m^{k}_{GSC}(t)\right] \tag{20}$$

where k is the dq components reference frame vector of the grid side VSC, m^{k}_{GSC} is the modulated index vector.

Making $L_{GSC} = L^{d}_{GSC} = L^{q}_{GSC}$, the presence of $\omega_0 L_{GSC}$ in (19) indicates the coupled dynamics between i^{d}_{GSC} and i^{q}_{GSC}. Decoupling these dynamics m^{d}_{GSC} and m^{q}_{GSC} are changed, based in the dq reference frame, i.e.

$$\left[m^{d}_{GSC}(t)\right] = \left(2/V_{DC}(t)\right)\left[\mathrm{E}^{d}_{GSC}(t) - \left(\left(\omega_{0}\cdot L_{GSC}\right)i^{q}_{GSC}(t)\right) + v^{d}_{WES}(t)\right] \tag{21a}$$

$$\left[m^{q}_{GSC}(t)\right] = \left(2/V_{DC}(t)\right)\left[\mathrm{E}^{q}_{GSC}(t) + \left(\left(\omega_{0}\cdot L_{GSC}\right)i^{d}_{GSC}(t)\right) + v^{q}_{WES}(t)\right] \tag{21b}$$

where $E^{d}_{GSC}(t)$ and $E^{q}_{GSC}(t)$ are two additional control inputs.

The GSC plant is obtained by substituting (21) into (20), subsequently, (20) is replacing into (19) generating a first order lineal system, this in Equation (22) is described.

$$L_{GSC}\left[di^{k}_{GSC}(t)/dt\right] = \left[\mathrm{E}^{k}_{GSC}(t)\right] - R_{GSC}\left[i^{k}_{GSC}(t)\right] \tag{22}$$

Peer-reviewed version available at Energies 2018, 11, 2458; doi:10.3390/en11092458

The frequency domain of the Equation (22) is shown in (23); which describe a decoupled, first-order, linear system, controlled through $E_{GSC}^{k}(s)$; also, Equation (23) representing the grid side VSC plant.

$$\left[i_{GSC}^{k}(s)\right]=\left[\mathrm{E}_{GSC}^{k}(s)\right]\left(sL_{GSC}+R_{GSC}\right)^{-1} \tag{23}$$

With the purpose of tracking the $i_{GSC}^{k}(s)$ reference commands in the closed loop, the proportional-integral (PI) compensators are used, obtaining:

$$\left[\mathrm{E}_{GSC}^{k}(s)\right]\approx\left[k_{GSC}^{k}(s)\right]=\left[\frac{\left(\alpha_{GSC}skp_{GSC}^{k}+\alpha_{GSC}ki_{GSC}^{k}\right)}{\alpha_{GSC}s}\right]=\left[\left(\frac{\alpha_{GSC}}{s}\right)\left(\frac{\left(skp_{GSC}^{k}+ki_{GSC}^{k}\right)}{\alpha_{GSC}}\right)\right] \tag{24}$$

where kp_{GSC}^{k} and ki_{GSC}^{k} are the proportional and integral gains, respectively.

The feedback loop $\iota_{GSC}^{k}(s)$ is:

$$\left[\iota_{GSC}^{k}(s)\right]=\left[i_{GSC}^{kref}(s)-i_{GSC}^{k}(s)\right]=\left[\left(\frac{\alpha_{GSC}}{s}\right)\left(\frac{\left(skp_{GSC}^{k}+ki_{GSC}^{k}\right)}{\alpha_{GSC}}\right)\left(\frac{1}{sL_{GSC}+R_{GSC}}\right)\right] \tag{25}$$

The relation between the plant pole and the PI compensator zero is obtained in (26), generating the kp_{GSC}^{k} and ki_{GSC}^{k} control gains.

$$\left[kp_{GSC}^{k}\right]=\left[\alpha_{GSC}L_{GSC}\right]=\left[\left(2.2/\tau_{GSC}\right)L_{GSC}\right] \tag{26a}$$

$$\left[ki_{GSC}^{k}\right]=\left[\alpha_{GSC}R_{GSC}\right]=\left[\left(2.2/\tau_{GSC}\right)R_{GSC}\right] \tag{26b}$$

where τ_{GSC} is selected from 5ms to 0.5ms based on the transferred power.

2.4. The DC-side control of the AFE converter.

GSC improves the DC-link control. The time-domain relationship of the DC-link of the AFE converter is given by:

$$\left[dV_{DC}(t)/dt\right]=\left[I_{DC}(t)/C_{DC}\right]-\left[V_{DC}(t)/\left(C_{DC}\cdot R_{DC}\right)\right] \tag{27}$$

The sum of currents entering to the capacitor is:

$$\left[I_{DC}(t)\right]=\frac{1}{2}\sum_{l=a}^{c}m_{GSC}^{l}(t)\left[i_{GSC}^{l}(t)\right] \tag{28}$$

The functionality of the AFE converter requires that:

$$V_{DC}\geq\left|2\left(v_{WESL-L}\right)\right| \tag{29}$$

The DC-link control is calculated through the stored energy in the capacitor, that is,

$$\left[U_{DC}(s)\right]=\left(C_{DC}/2\right)\left[V_{DC}^{2}(s)\right] \tag{30}$$

where U_{DC} is the stored energy in the capacitor and C_{DC} is the DC-link capacitance.

Considering that $U_{DC}(s)\approx P_{GSCref}(s)$ and using the d reference frame component of grid side VSC plant described in (22) the DC-link control is made, generating the active power control, that is:

$$\left[P_{GSCref}(s)\right]=\left(C_{DC}/2\right)\left[V_{DCref}^{2}(s)-V_{DC}^{2}(s)\right]\left[E_{GSC}^{d}(s)\right] \tag{31}$$

The reactive power control is made with the q reference frame component of GSC plant described in (22), that is,

$$\left[Q_{GSCref}(s)\right]=\left[Q_{WESref}(s)-Q_{WES}(s)\right]\left[\mathrm{E}_{GSC}^{d}(s)\right] \tag{32}$$

where Q_{WES} is the presented reactive power at the WES.

It is important to consider that, the subscript τ_{WES} presented in (32) must be at least ten times higher than τ_{GSC}.

Preprints (www.preprints.org) | NOT PEER-REVIEWED | Posted: 4 September 2018 doi:10.20944/preprints201809.0054.v1

Peer-reviewed version available at Energies 2018, 11, 2458; doi:10.3390/en11092458

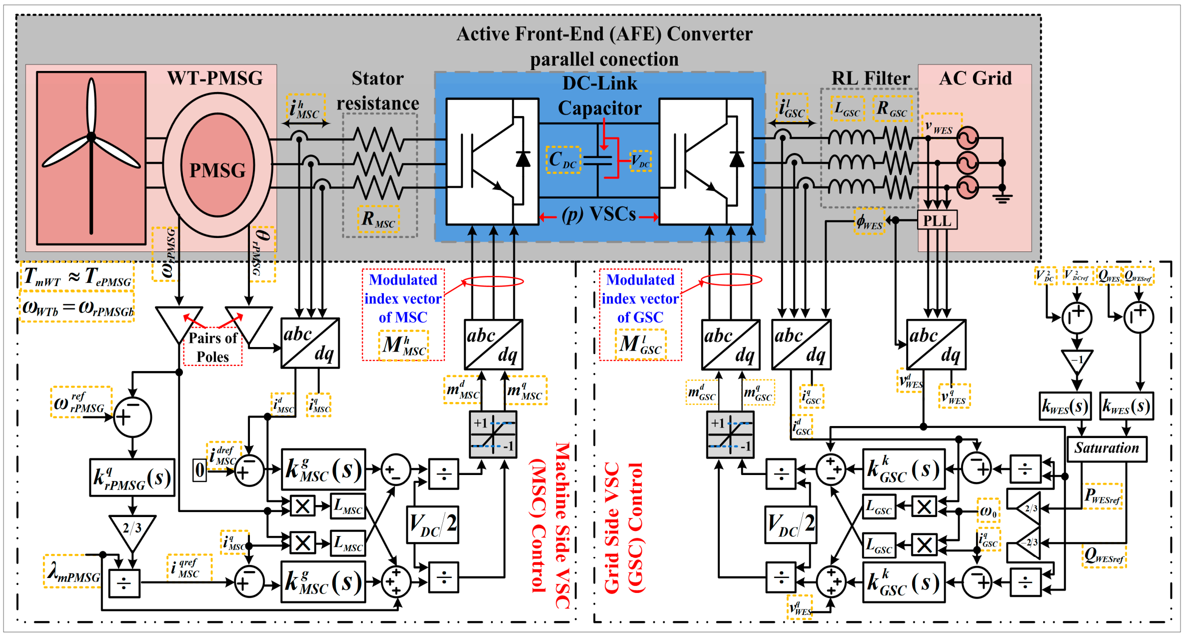

Figure 2 Modeling control of WES

2.4. System parameters design of the AFE converter

The correct operation of the type-4 WT control depends on the precise design of the AFE converter parameters; thus, the elements values of the MSC are obtained from the WT-PMSG nominal power, $P_{WT\text{-}PMSG}$, that is: the current is $i_{MSC} = (2/3)(P_{WT\text{-}PMSG}/v_{MSC})$; the machine side impedance is $Z_{MSCt}=v_{MSC}/i_{MSC}$ thus, the MSC works with 15% of the total WT-PMSG impedance, i.e.: $Z_{MSC}=(0.15)Z_{MSCt}$; from the WT-PMSG characteristics are taken the next parameters: L_{MSC}, R_{MSG}, D, H. The elements values of the GSC are obtained from the WES nominal power, but making $P_{WES} = P_{WT\text{-}PMSG}$ is generated i_{GSC} using $i_{MSC} = (2/3)(P_{WES}/v_{GSC})$; the grid side impedance is $Z_{GSCt}=v_{GSC}/i_{GSC}$ the GSC works with 15% of the total WES impedance, i.e.: $Z_{GSC} = (0.15)Z_{GSCt}$; therefore, L_{GSC} is calculated with $L_{GSC} = Z_{GSC}/\omega_0$ the R_{GSC} value varies according to the transferred power, in a range from 0.1Ω to 0.5Ω; the base WES capacitance CW_{ES} is calculated with $C_{WES} = 1/(Z_{GSC}\omega_0)$. Then, a better time response in the WES feedback is achieved, since the L_{MSC} and R_{MSC} values are used in (10), H and D values are used in (17), L_{GSC} and R_{GSC} values are used in (26), to obtain the system feedback gains.

It is important to establish that, from the generated active power by the GSC, v_{WES} is kept constant in the presence of any perturbation; for which, it is essential to calculate the correct capacitance value that maintains the DC-link compensation, this is determined from the base DC-link capacitance, i.e, $C_{DC}=(3/8)C_{WES}$, determining the store energy in (30).

3. Modeling of the DSPWM Technique Applied in the THD Reduction

Digital modulation techniques are the most generalized framework in the control of modern power electronics converters applications. Digital sinusoidal pulse width modulation (DSPWM) is a modulation technique created by the internal generation of the modulated and carrier signals using a digital controller [22]. THD reduction is achieved by modifying the DSPWM switching signals in each VSC. This is carried out applying a different phase shift angle in each carrier signals of each VSC; the modulated signal angle is not changed. Then, the output signals (voltage or current) of each VSC are added. In this paper, the AFE converter is built with three VSC connected in parallel, the DSPWM is shown in Figure 3.

Preprints (www.preprints.org) | NOT PEER-REVIEWED | Posted: 4 September 2018 doi:10.20944/preprints201809.0054.v1

Peer-reviewed version available at Energies 2018, 11, 2458; doi:10.3390/en11092458

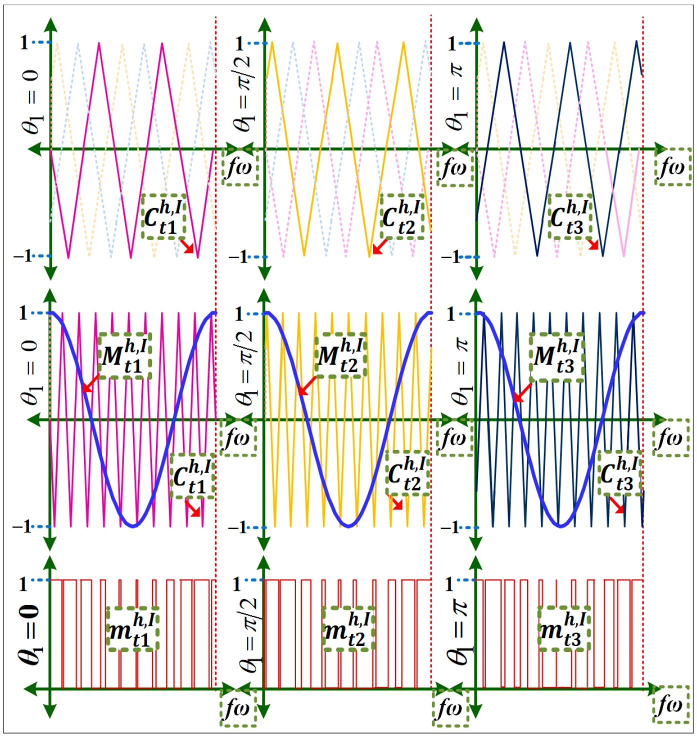

Figure 3 DSPWM signal applied to each VSC connected in parallel (phase a).

Figure 3 shows the comparison between the modulated (without phase shift angle) and carrier (with phase shift angle) signals, generating the DSPWM signal (phase a) corresponding to each VSC connected in parallel. The correct phase shift angle between each carrier signal is established putting up different values of total phase shift angle at the WES (Figure 2), the analysis in Table 1 is shown.

Table 1 Analysis of different phase shift at the carrier signal.

Total phase shift (θ_p)	Carrier phase shift in each VSC θ_1	θ_2	θ_3	%Total Harmonic Distortion (THD)
0	0	0	0	6.8%
π/6	0	π/18	π/9	4.33%
π/3	0	π/9	2π/9	1.99%
π/2	0	π/6	π/3	2.054%
2π/3	0	2π/9	4π/9	1.271%
5π/6	0	5π/18	5π/9	1.608%
π	0	π/3	2π/3	4.616%
7π/6	0	7π/18	7π/9	5.635%
4π/3	0	4π/9	8π/9	2.864%
3π/2	**0**	**π/2**	**π**	**1.239%**
5π/3	0	5π/9	10π/9	1.36%
11π/6	0	11π/18	11π/9	1.867%
2π	0	2π/3	4π/3	2.756%

Through Table 1 it is observed that the angle that generates a lower THD is 3π/2; hence, this angle divides the number of VSCs placed in parallel, i.e.:

$$\theta_p = (3\pi/2)\big/p \tag{33}$$

where p is the number of VSC connected in parallel and θ_p is the carrier signal phase shift angle of each VSC.

The n-harmonics content is calculated through the Fourier series expansion, i.e.,

$$F(t) = C_0 + \sum_{n=1}^{\infty}\left(C^n_{MSC,GSC}\cos\left(n\omega_0 t + \sigma\right)\right) \tag{34}$$

where n is the harmonic number, $C^n_{MSC,GSC} = \sqrt{(a^n_{MSC,GSC})^2 + (b^n_{MSC,GSC})^2}$, $\sigma = \tan^{-1}(b^n_{MSC,GSC}\big/a^n_{MSC,GSC})$ and $C_0 = a_0\big/2$.

The magnitude of each harmonic is calculated by,

Peer-reviewed version available at Energies 2018, 11, 2458; doi:10.3390/en11092458

$$a^{n}_{MSC,GSC}=\frac{2}{T}\left(\int_{-T/2}^{T/2}F(t)\cos(n\omega_0 t)\,d\omega_0 t\right) \tag{35}$$

$$b^{n}_{MSC,GSC}=\frac{2}{T}\left(\int_{-T/2}^{T/2}F(t)\sin(n\omega_0 t)\,d\omega_0 t\right) \tag{36}$$

To calculate the THD in the AFE converter, the individually equivalent circuit of each three-phase VSC is analyzed.

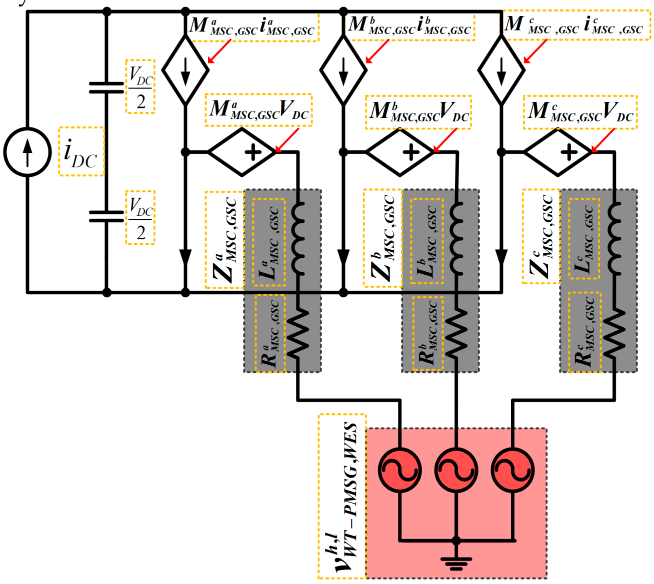

Figure 4 Three-phase VSC equivalent circuit

Three-phase VSC equivalent circuit is shown in Figure 4 and this is represented by the next equation,

$$\begin{bmatrix} 2(Z*i^{a}) & -(Z*i^{b}) & -(Z*i^{c}) \\ -(Z*i^{a}) & 2(Z*i^{b}) & -(Z*i^{c}) \\ -(Z*i^{a}) & -(Z*i^{b}) & 2(Z*i^{c}) \end{bmatrix}_{MSC,GSC} = \left[\begin{pmatrix} v^{a}-v^{b} \\ v^{b}_{b}-v^{c} \\ v^{c}-v^{a} \end{pmatrix}_{MSC,GSC} - \begin{pmatrix} v^{a}-v^{b} \\ v^{b}-v^{c} \\ v^{c}-v^{a} \end{pmatrix}_{WT-PMSG,WES}\right] \tag{37}$$

Using Kirchhoff's current law (KCL), the currents flowing towards the MSC or/and GSC node must be equal to the currents leaving the MSC or/and GSC node, i.e.,

$$i^{c}_{MSC,GSC}=-\left(i^{a}_{MSC,GSC}+i^{b}_{MSC,GSC}\right) \tag{38}$$

Replacing equation (38) in (37) gives line-to-line current of the MSC or/and GSC, i.e.

$$\begin{bmatrix} i^{ab}_{MSC,GSC} \\ i^{bc}_{MSC,GSC} \\ i^{ca}_{MSC,GSC} \end{bmatrix} = \left(\frac{1}{3Z^{h,l}_{MSC,GSC}}\right)\left(\begin{bmatrix} v^{a}_{b}-v^{b} \\ v^{b}-v^{c} \\ v^{c}-v^{a} \end{bmatrix}_{WT-PMSG,WES} - \begin{bmatrix} v^{a}_{b}-v^{b} \\ v^{b}-v^{c} \\ v^{c}-v^{a} \end{bmatrix}_{MSC,GSC}\right) \tag{39}$$

where $v_{WT\text{-}PMSG}$ represents the WT-PMSG voltage, v_{WES} exemplifies the WES voltage, $v_{MSC,GSC}$ is the VSC AC-side output voltage of MSC or/and GSC and $Z^{h,l}_{MSC,GSC}$ is the AC-side filter of MSC or/and GSC.

The $v_{MSC,GSC}$ value depends on $M^{h,l}_{MSC,GSC}$ signal modulation. The modulated and carrier signals implement the DSPWM technique of Figure 3; these have modulation frequencies of 60Hz (ω_0) and 7kHz ($f\omega$), respectively.

The carrier signal is composed by an up-slope and a down-slope, calculated as,

$$C_{t_1 p}=1-\left(\left(4/f\omega\right)\left(\omega_0 t_1-\theta_p\right)\right) \tag{40}$$

$$C_{t_2 p}=\left(\left(4/f\omega\right)\left(\omega_0 t_2-\left(f\omega/2\right)-\theta_p\right)\right)-1 \tag{41}$$

where $C_{t1,t2p}$ is the composed carrier signal, θ_p is phase shift angle of each VSC, $f\omega$ is switching frequency of the carrier signal, t_1 is the time for the up-slope, t_2 is the time for the down-slope.

Time t_1 for up-slope is

$$\theta_p \le t_1 \le \left(\left(f\omega/2\right)+\theta_p\right) \tag{42}$$

Time t_2 for down-slope is:

$$\left(\left(f\omega/2\right)+\theta_p\right) \le t_2 \le \left(f\omega+\theta_p\right) \tag{43}$$

Preprints (www.preprints.org) | NOT PEER-REVIEWED | Posted: 4 September 2018 doi:10.20944/preprints201809.0054.v1

Peer-reviewed version available at Energies 2018, 11, 2458; doi:10.3390/en11092458

Modulated signals in each VSC are described by the carrier signal time, that is:

$$\begin{aligned} M_{t_1 p}^{h,l} &= \cos(t_1+\varphi) \\ M_{t_2 p}^{h,l} &= \cos(t_2+\varphi) \end{aligned} \quad (44)$$

where $h,l = a,b,c$ the VSC phases in MSC and GSC, respectively and φ is the corresponding angle of each phase in the modulated signal.

The comparison between modulated and carrier signals defines the DSPWM signal, its representation is:

$$\begin{aligned} DSPWM_{t_1 p}^{h,l} &= \left| M_{t_1 p}^{h,l} \le C_{t_1 p} \right| \\ DSPWM_{t_2 p}^{h,l} &= \left| M_{t_2 p}^{h,l} \le C_{t_2 p} \right| \end{aligned} \quad (45)$$

Multiplying the DSPWM signal and DC voltage amplitude generates the VSCs output voltage for each phase value in MSC and GSC, i.e,

$$v_{MSC,GSC}^{h,l} = V_{DC} * DSPWM_{MSC,GSC}^{h,l} \quad (46)$$

The WT-PMSG voltage $v_{WT-PMSG}^{h}$ is generated by,

$$\begin{aligned} v_{t_1 WT-PMSG}^{h} &= PMSG\left(\cos\left(\omega_{rPMSG} t_1 + \theta_{rPMSG}\right)\right) \\ v_{t_2 WT-PMSG}^{h} &= PMSG\left(\cos\left(\omega_{rPMSG} t_2 + \theta_{rPMSG}\right)\right) \end{aligned} \quad (47)$$

where *PMSG* is the WT-PMSG amplitude voltage and ϕ is the corresponding angle of each phase in the three-phase WT-PMSG.

And the WES voltage v_{WES}^{l} is produced by,

$$\begin{aligned} v_{t_1 WES}^{l} &= WES\left(\cos\left(\omega_0 t_1 + \phi_{WES}\right)\right) \\ v_{t_2 WES}^{l} &= WES\left(\cos\left(\omega_0 t_2 + \phi_{WES}\right)\right) \end{aligned} \quad (48)$$

where *WES* is AC grid amplitude voltage and ϕ_{WES} is the corresponding angle of each phase in the three-phase WES grid.

The output current in each VSC is calculated as,

$$\begin{aligned} \left[i_{t_1 MSC,GSC}^{h,l} \right] &= \left(1/\left(3Z_{MSC,GSC}\right)\right)\left(\left[v_{t_1 WT-PMSG,WES}^{h,l} \right] - \left[v_{t_1 MSC,GSC}^{h,l} \right]\right) \\ \left[i_{t_2 MSC,GSC}^{h,l} \right] &= \left(1/\left(3Z_{MSC,GSC}\right)\right)\left(\left[v_{t_2 WT-PMSG,WES}^{h,l} \right] - \left[v_{t_2 MSC,GSC}^{h,l} \right]\right) \end{aligned} \quad (49)$$

The harmonic content spectrum to obtain the THD is required. By using (35), (36) and (49) the spectrum is calculated as,

$$a_{MSC,GSC}^{n} = \left(\frac{2}{T}\right)\left[\left(\int_{\theta_p}^{(f\omega/2)+\theta_p}\left(i_{t_1 MSC,GSC}^{h,l}\cos\left(n\omega_0 t_1\right)\right)d\omega_0 t_1\right) + \left(\int_{(f\omega/2)+\theta_p}^{f\omega+\theta_p}\left(i_{t_1 MSC,GSC}^{h,l}\cos\left(n\omega_0 t_2\right)\right)d\omega_0 t_2\right)\right] \quad (50)$$

$$b_{MSC,GSC}^{n} = \left(\frac{2}{T}\right)\left[\left(\int_{\theta_p}^{(f\omega/2)+\theta_p}\left(i_{t_1 MSC,GSC}^{h,l}\sin\left(n\omega_0 t_1\right)\right)d\omega_0 t_1\right) + \left(\int_{(f\omega/2)+\theta_p}^{f\omega+\theta_p}\left(i_{t_2 MSC,GSC}^{h,l}\sin\left(n\omega_0 t_2\right)\right)d\omega_0 t_2\right)\right] \quad (51)$$

For the harmonic content of the output current signal, the magnitude of the individual harmonics is calculated for each VSC connected in parallel of the MSC and GSC and these are added, i.e.

$$a_{MSC,GSC}^{n1} + a_{MSC,GSC}^{n2} + \ldots + a_{MSC,GSC}^{np} \quad (52)$$

$$b_{MSC,GSC}^{n1} + b_{MSC,GSC}^{n2} + \ldots + b_{MSC,GSC}^{np} \quad (53)$$

where p is the number of VSCs placed in parallel and n is the number of harmonics.

The THD in the AFE converter output current is,

$$THDi_{MSC,GSC}^{h,l} = \left| \left(\frac{1}{C_{MSC,GSC}^{1p}}\right)\sqrt{\sum_{n=2}^{\infty}\left(C_{MSC,GSC}^{np}\right)^2} \right| * 100 \quad (54)$$

where $C_{MSC,GSC}^{1p}$ is the fundamental harmonic magnitude and $C_{MSC,GSC}^{np}$ is the n harmonic magnitude.

Finally, the lower THD content in the output current of AFE converter is generated when the output current signals of each VSC are added, i.e.

$$i_{MSC,GSC}^{h,l} = i_{MSC1,GSC1}^{h,l} + i_{MSC2,GSC2}^{h,l} + \ldots + i_{MSCp,GSCp}^{h,l} \quad (55)$$

4. Simulation Results: Study Case for WES

In this paper, Matlab-Simulink® and Opal-RT Technologies® module (OP-5600) are the main elements in the WES real time simulation, since the OP-5600 module uses the rapid control

Peer-reviewed version available at Energies 2018, 11, 2458; doi:10.3390/en11092458

prototyping (RCP) concept, which allows testing the control law without needing any programming code.

In Figure 2 the simulated WES is shown. It contains a WT-PMSG to supply the MSC, the AFE parallel converter and the infinite bus (considered as an ideal voltage source) to supply the GSC. The MSC and GSC are connected to WT-PMSG and the AC grid through a RL filters, both converters are formed by three VSCs connected in parallel and each one is designed at power and voltage of 2MVA and 2.5kV, respectively. The characteristics of the WT-PMSG are described in the Table 2.

Table 2 WT-PMSG characteristics.

Wind Turbine (WT)			
Nominal output power	2 MW	*Base wind speed*	12 m/s
Pitch angle	45 deg	*base generator speed*	1.2 pu
Permanent Magnet Synchronous Generator (PMSG)			
Mechanical input	-8.49e5 N.m.	*Stator resistance*	8.2e-4 Ω
Armature inductance	1.6e-3 H	*Flux linkage*	5.82
Viscous damping	4.04e3 N.m.s	*Inertia*	2.7e6 kg.m^2
Pole pairs	4	Rotor type	Round

To verify the correct WES operation of Figure 2, in Figure 5 the behavior of the WT mechanical torque and the PMSG electric torque are analyzed.

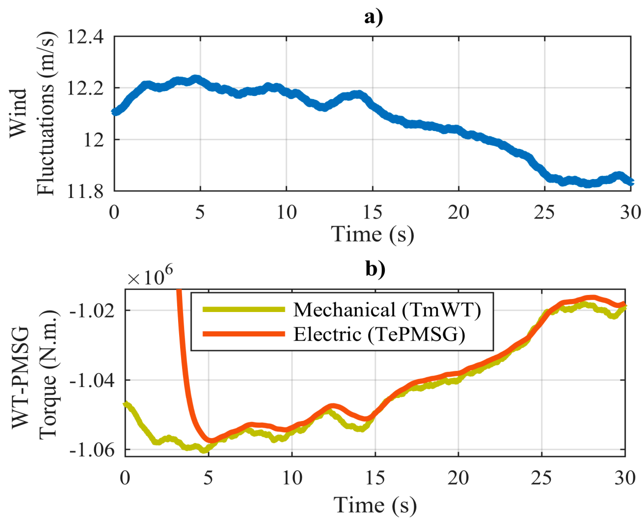

Figure 5 behavior of the WT mechanical torque and the PMSG electric torque in the presence of wind fluctuations. a) Wind fluctuations; b) Mechanical and Electric torque.

Figure 5 a) contents the wind fluctuations applied to the WT, which are generated in Matlab-Simulink® by a rotor wind model developed by RISOE National Laboratory based on Kaimal spectra. Figure 5 b) shows the behavior of the WT mechanical torque and the PMSG electric torque in the presence of wind fluctuations of Figure 5 a). It is possible to see that, the electric torque follows the mechanical torque behavior, due the effective structure of the MSC closed loop control.

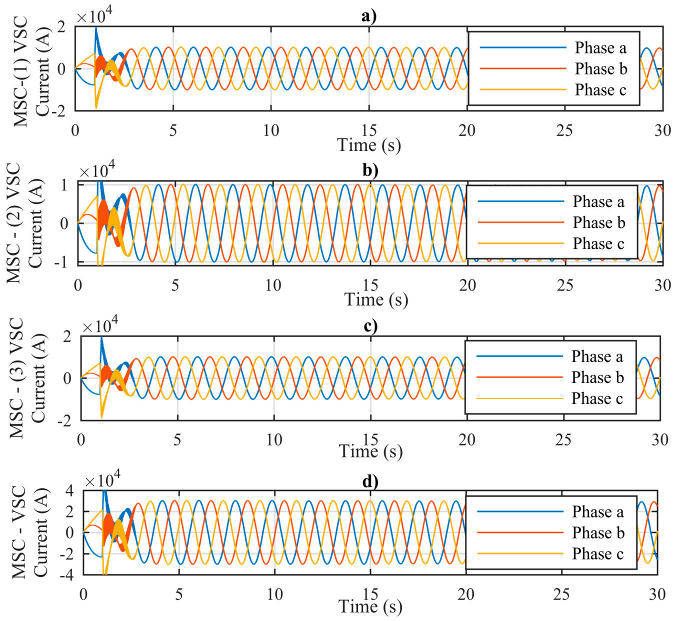

Figure 6 Current present in MSC of AFE parallel converter. a) (1) VSC; b) (2) VSC; c) (3) VSC; d) Total current.

Figure 6 shows the generated current by the WT-PMSG, that through the MSC of AFE parallel converter is controlled. Due to the MSC is formed using the parallel connection of three VSCs, then each VSC can handle one third of the total current generated by the WT, Figures 6 a) b) c) illustrate the current in the (1) (2) (3) VSC, respectively; and in Figure 6 d) the MSC total current is shown. While, the main MSC function is the rotor flux frequency control, generating the power conversion between medium AC voltage and low DC voltage levels, the most important GSC function is to keep the DC-link constant, transferring the generated power between the WT-PMSG and AC grid in the required voltages by the consumers

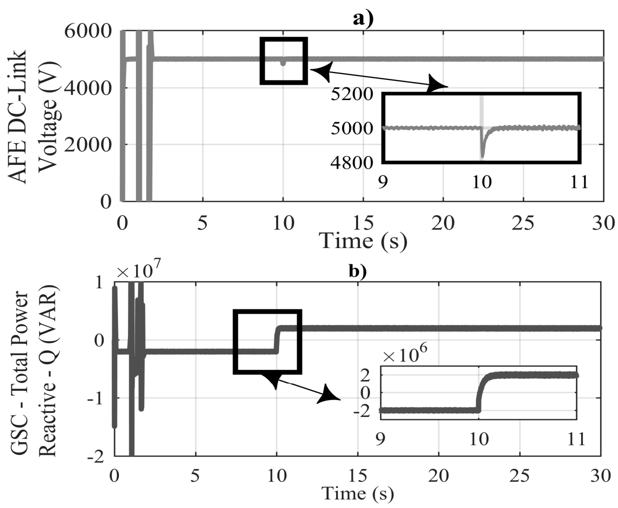

Figure 7 DC-Link and Reactive Power controlled by the GSC. a) DC-link voltage; b) Exchange of reactive power in WES.

Preprints (www.preprints.org) | NOT PEER-REVIEWED | Posted: 4 September 2018 doi:10.20944/preprints201809.0054.v1

Peer-reviewed version available at *Energies* **2018**, *11*, 2458; doi:10.3390/en11092458

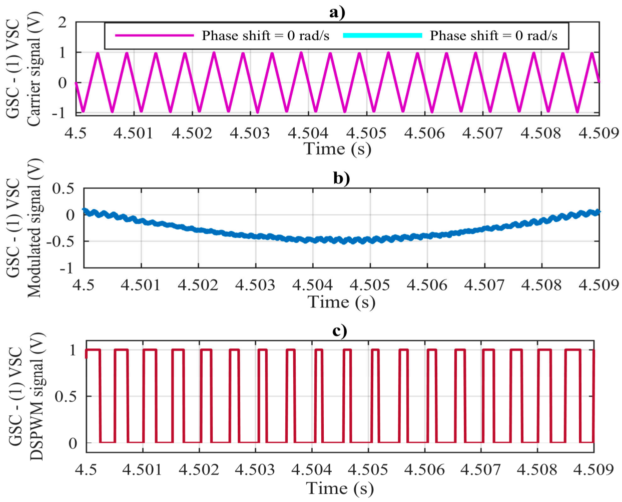

Figure 8 DSPWM signal applied to the control of the first VSC connected in parallel in GSC. a) Carrier signal; b) Modulated signal; c) DSPWM.

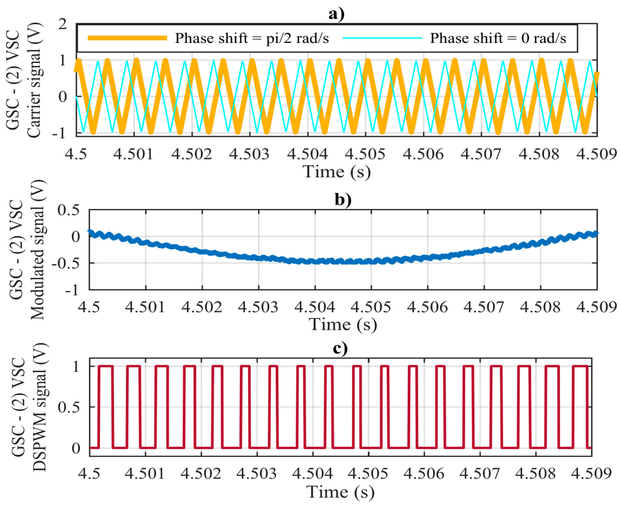

Figure 9 DSPWM signal applied to the control of the second VSC connected in parallel in GSC. a) Carrier signal; b) Modulated signal; c) DSPWM.

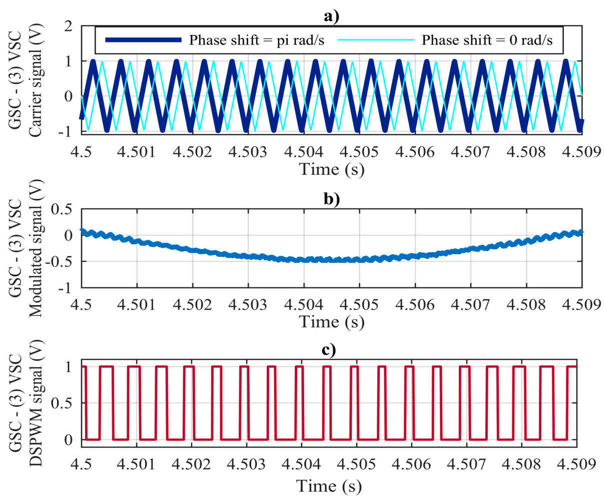

Figure 10 DSPWM signal applied to the control of the third VSC connected in parallel in GSC. a) Carrier signal; b) Modulated signal; c) DSPWM.

Then, in the Figure 7 a) can be observed that, the DC-link remains constant at 5kV, because, when the MSC requires a reactive power exchange, due to the wind fluctuations of Figure 5 a), the

GSC restores the DC-Link, and at the same time injects the needed reactive power, as shown in Figure 7 b).

Figures 8, 9 and 10 content the applied DSPWM to each of the VSC connected in parallel for the GSC correct operation, at the stability time since 4.5ms to 4.509ms. In Figure 8 can be seen that, both the carrier signal of Figure 8 a) and the modulated signal of Figure 8 b) start at the same time, i.e. the carrier signal does not present any phase shift, generating the DSPWM signal in Figure 8 c), this is applied to the first VSC connected in parallel in the GSC. In Figure 9, the DSPWM generation applied to the second VSC connected in parallel of the GSC is shown; in Figure 9 a) can be observe a phase shift of π/2 (rad/s) in carrier signal, this is compared with the modulated signal of Figure 9 b), originating the DSPWM with phase shift of Figure 9 c). Finally, in Figure 10, the DSPWM signal applied to the third VSC connected in parallel of the GSC is presented; in Figure 10 a) the carrier is observed with a phase shift of π (rad/s) respect of the modulated of Figure 10 b), generating the DSPWM of Figure 10 c).

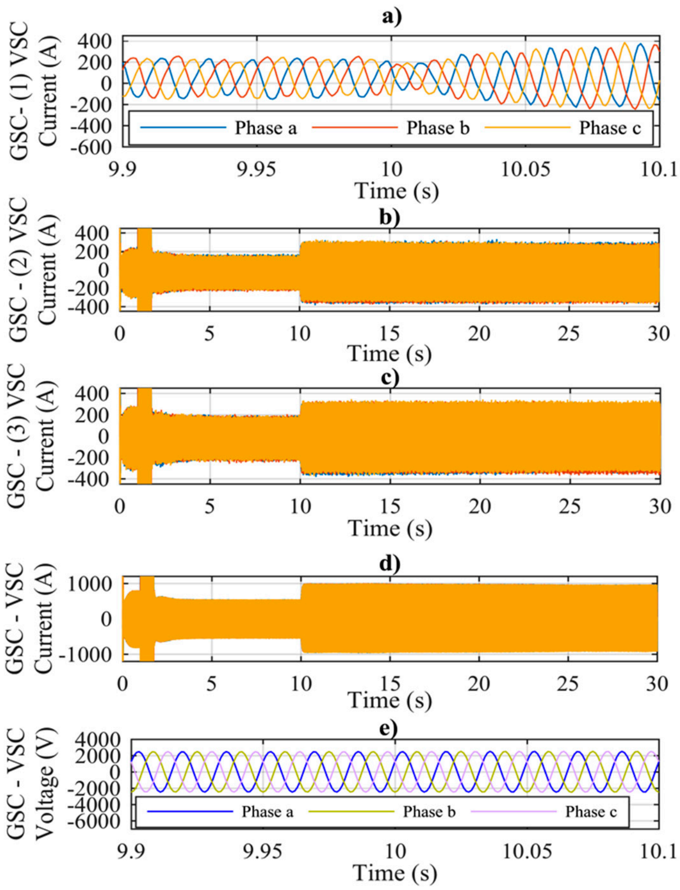

Figure 11 Electrical variables generated by the GSC. a) Zoom of the handled current at the (1) VSC; b) The handled current at the (2) VSC; c) The handled current at the (3) VSC; d) Total current; e) Zoom at the magnitude voltage.

Figure 11 shows the electrical variables present at the GSC when the corresponding phase shift in the carriers of each VSC connected in parallel are performed, according to Equation (33). Figure 11 a) shows the (1) VSC current generated due the phase shift at the carrier of Figure 8 a); in which, a zoom in time is made from 9.9s to 10.1s, observing the current magnitude and behavior in the presence of reactive power exchange at Figure 7 b). Figure 11 b) shows the (2) VSC current generated due the phase shift at the carrier of Figure 9 a); Figure 11 c) shows the (3) VSC current generated due the phase shift at the carrier of Figure 10 a); in Figures 11 a), b) and c) each current magnitude is 330A, generating a total GSC current of 990A, as see in Figure 11 d); Figure 11 e) contents a zoom in time from 9.9s to 10.1s, observing the generated voltage at the GSC, whose magnitude corresponds to 2500V.

Preprints (www.preprints.org) | NOT PEER-REVIEWED | Posted: 4 September 2018 doi:10.20944/preprints201809.0054.v1

Peer-reviewed version available at *Energies* **2018**, *11*, 2458; doi:10.3390/en11092458

Finally, the current THD is shown in Figure 12; Figure 12 a) contents the THD without any phase shift between carriers of each VSC of the AFE converter, which corresponds to 6.8%. Please observe that, in Figure 12 b), when the corresponding phase shift is performed in the carriers, the current THD is reduced to 1.239%, as specified in Table 1. The Figure shows the harmonics magnitude reduction or even their elimination, once the phase shift between carriers is made. The THD was reduced in approximately 5.5 times.

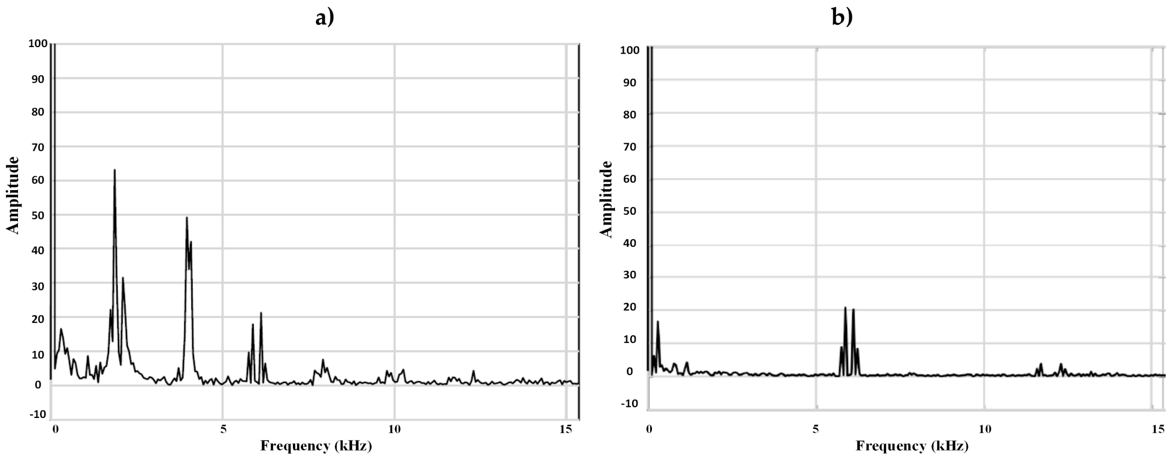

Figure 12 THD present at the WES. a) Without phase shift between carriers of each VSC; b) With phase shift between carriers of each VSC.

4. Real Time Simulation Results: Study Case for WES using Opal-RT Technologies®

To verify the robustness to the applied control in the AFE converter and the THD reduction at the WES, the grid of Figure 2 in real time using the Opal-RT Technologies® is simulated. Initially, it is necessary to specify that a switching frequency of 7kHz is used in the IGBTs that constitute each VSC of the AFE converter. Figure 13 a) shows the wind fluctuations generated by a rotor wind model developed by RISOE National Laboratory based on Kaimal spectra. Figure 13 b) contains the mechanical torque behavior generated by the wind turbine, and in response to the applied control at the MSC, the PMSG electric torque is able to follow the same behavior.

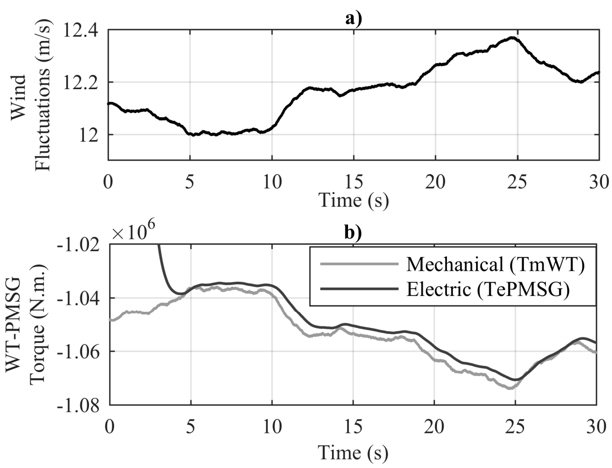

Figure 13 Behavior of the WT mechanical torque and the PMSG electric torque in the presence of wind fluctuations simulated in the Opal-RT Technologies®. a) Wind fluctuations; b) Mechanical and Electric torque.

Figure 14 presents the main electrical variables at the WES simulated in real time by OPAL-RT®. Figure 14 a) contains the current portion that handles the first VSC connected in parallel; as can be seen, due that only three VSCs are connected in parallel, each one handles only a third of the total current generated by the MSC, the total current in Figure 14 b) is presented and this is transferred by the WT-PMSG to the AC grid through the AFE converter. In Figure 14 c) the generated voltage by the MSC is observed. It is important to say that, the GSC main objective is support the constant DC-link in the presence of any disturbance (such as: voltage / current variations

Preprints (www.preprints.org) | NOT PEER-REVIEWED | Posted: 4 September 2018 doi:10.20944/preprints201809.0054.v1

Peer-reviewed version available at *Energies* **2018**, *11*, 2458; doi:10.3390/en11092458

due to wind fluctuations or reactive power exchanges by the behavior of the WT), this can be proved in Figure 14 d) and this is possible due to the applied control robustness. Figure 14 e) shows the GSC ability to exchange reactive power, that is, it is possible the injection / absorption of 6 MVA into the AC grid. Figure 14 f) contains the handled current portion by the first VSC connected in parallel at the GSC; similarly, due that only three VSCs are connected in parallel, each one handles only a third of the total current generated by the GSC; in Figure 14 g) the total current is presented. Finally, in Figure 14 h) the handled voltage by the GSC is observed, which this is taken from the PCC attached to the AC grid. The THD of the handled total current by the GSC is generated through the OPAL-RT®. The generated THD without phase shift between the carriers of each VSC connected in parallel, this corresponds to 8.85%. The produced THD once the phase shift between the carriers of each VSC is made, which corresponds to 2.18%, the phase shift from equation (33) is calculated; therefore it is demonstrated that, making the WES real-time simulation and applying the phase shift between the carriers of each VSC, the THD can be reduced up four times.

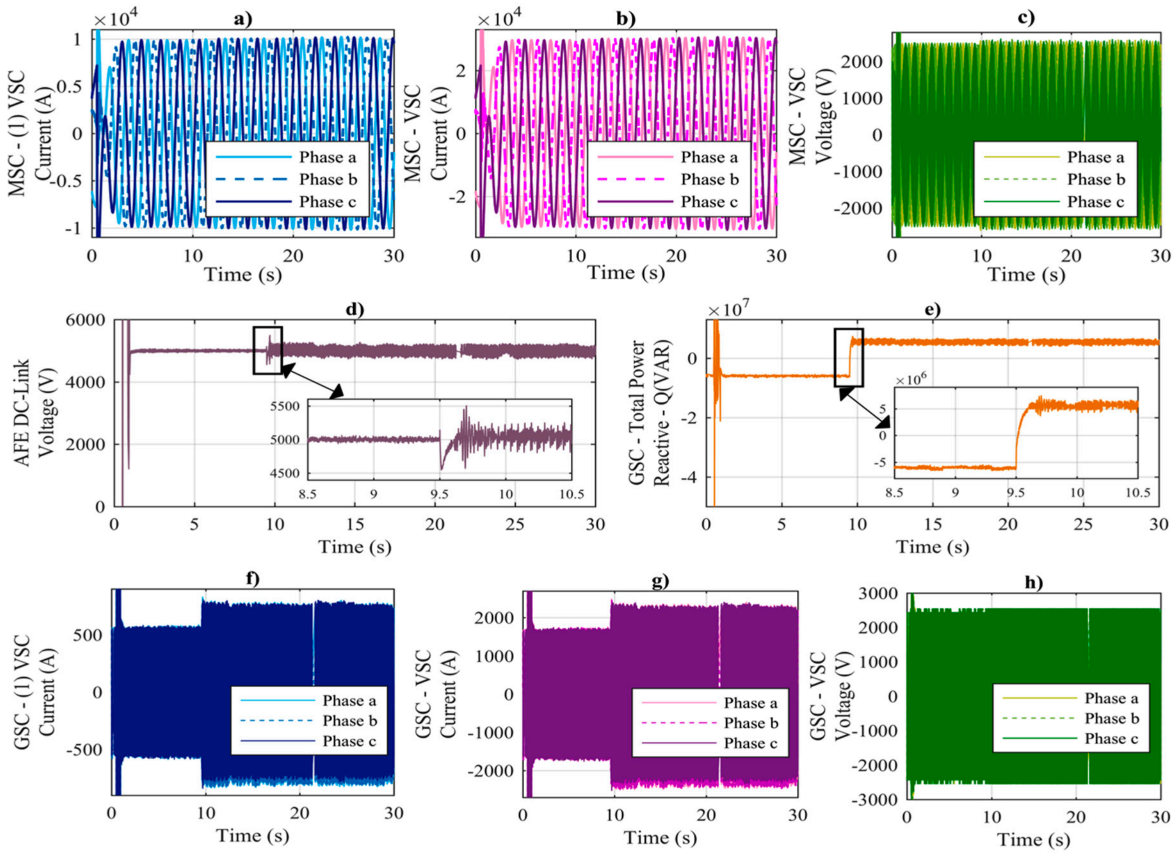

Figure 14 Electrical variables generated at the WES simulated in the Opal-RT Technologies®. a) The handled current by the (1) VSC of MSC. b) Total current handled by the MSC; c) Voltage present at the MSC; d) DC-Link voltage controlled by the GSC; e) Reactive Power controlled by the GSC; f) The handled current by the (1) VSC of GSC; g) Total current handled by the GSC; h) Voltage present at the GSC.

Finally, it is important to mention that, the block –*written to file*– produces the results of Figures 13–14 in the MATLAB–Simulink® interface; this allows plotting the variables in MATLAB windows in order to have a better presentation.

5. Conclusions

In this paper, A WES has been analyzed; which by a WT-PMSG connected to the AC grid through an AFE converter is designed. The AFE converter topology has been made from use a single VSC to use *p*VCS connected in parallel. This topology has been used for effective THD mitigation in a WES, through the variation in the DSPWM technique applied to each VSC, that is, a phase shift has been applied in each carrier signal angle of each VSC connected in parallel, while the modulated

Peer-reviewed version available at *Energies* **2018**, *11*, 2458; doi:10.3390/en11092458

signal angle has been keeping constant. A THD reduction up to 5.5 times has been generated at the total WES current output by Fourier series expansion.

To verify the robustness to the applied control, the WES control law has been simulated in real time, generating a rapid control prototyping (RCP) concept, which has been testing the WES dynamics without needing any programming code.

Acknowledgments: This work was supported in part by The National Council of Science and Technology (CONACYT) in Mexico, through the Scholarship awarded under the Called "***Estancias Posdoctorales Vinculadas a la Consolidación de Grupos de Investigación*".**

References

1. Shifeng Wang, K.; Sicong, W. Impacts of wind energy on environment: A review. *Renew. Sustain. Energy Rev.*, **2015**, *Vol. 49*, *pp. 437–443*. https://doi.org/10.1016/j.rser.2015.04.137
2. Salgado-Herrera, N. M.; Medina-Rios, A.; Tapia-Sánchez, R. Reactive Power Compensation in Wind Energy Systems through Resonant Corrector in Distributed Static Compensator. *Electric Power Components and Systems*, December **2017**, Volume 45, Issue 17, pp. 1859-1869. DOI: 10.1080/15325008.2017.1378947
3. Yaramasu, V.; Dekka, A.; Durán, M. J.; Kouro S.; Wu, B. PMSG-based wind energy conversion systems: survey on power converters and controls. *IET Electric Power Applications*, **2017**, vol. 11, no. 6, pp. 956-968, 7. **DOI:** 10.1049/iet-epa.2016.0799.
4. Renewable Energy (REN21): Global Status Report, Renewables 2017. Available at http://www.ren21.net/status-of-renewables/global-status-report/, accessed on November 2017.
5. Global Wind Energy Council (GWEC): Global Wind Report: Annual Market Update, April 2017. Available at http://www.gwec.net, accessed on January 2018.
6. Salgado-Herrera, N. M.; Medina-Ríos, A.; Tapia-Sánchez, R.; Anaya-Lara, O. Reactive power compensation through active back to back converter in type-4 wind turbine. *2016 IEEE International Autumn Meeting on Power, Electronics and Computing (ROPEC)*, Ixtapa, **2016**, pp. 1-6. **DOI:** 10.1109/ROPEC.2016.7830620.
7. Jlassi, I.; Estima, J. O.; Khojet El Khil, S.; Mrabet Bellaaj, N.; Marques Cardoso, A. J. Multiple Open-Circuit Faults Diagnosis in Back-to-Back Converters of PMSG Drives for Wind Turbine Systems. *IEEE Transactions on Power Electronics*, May **2015**, vol. 30, no. 5, pp. 2689-2702. **DOI:** 10.1109/TPEL.2014.2342506
8. Hu, W.; Chen, Z.; Wang, Y.; Wang, Z. Flicker Mitigation by Active Power Control of Variable-Speed Wind Turbines With Full-Scale Back-to-Back Power Converters. *IEEE Transactions on Energy Conversion*, Sept. **2009**, vol. 24, no. 3, pp. 640-649. **DOI:** 10.1109/TEC.2009.2015994
9. Lee, J. S.; Lee, K. B.; Blaabjerg, F. Open-Switch Fault Detection Method of a Back-to-Back Converter Using NPC Topology for Wind Turbine Systems. *IEEE Transactions on Industry Applications*, Jan.-Feb. **2015**, vol. 51, no. 1, pp. 325-335. **DOI:** 10.1109/TIA.2014.2327151
10. Nasiri, M.; Mohammadi, R. Peak Current Limitation for Grid Side Inverter by Limited Active Power in PMSG-Based Wind Turbines During Different Grid Faults. *IEEE Transactions on Sustainable Energy*, Jan. **2017**, vol. 8, no. 1, pp. 3-12. **DOI:** 10.1109/TSTE.2016.2578042
11. Juan, Y. L. Single switch three-phase ac to dc converter with reduced voltage stress and current total harmonic distortion. *IET Power Electronics*, May **2014**, vol. 7, no. 5, pp. 1121-1126. **DOI:** 10.1049/iet-pel.2013.0370
12. Ackermann, T. *Wind Power in Power Systems*, John Wiley & Sons Ltd, 2012, 2nd ed. pp. 203-204. ISBN 978 0 470 97416 2.
13. Salgado-Herrera, N. M.; Mancilla-David, F.; Medina-Ríos, A.; Tapia-Sánchez, R. THD mitigation in type-4 Wind Turbine through AFE Back to back converter. *2015 North American Power Symposium (NAPS)*, Charlotte, NC, **2015**, pp. 1-6. **DOI:** 10.1109/NAPS.2015.7335147
14. Hou, C. C.; Cheng, P. T. Experimental Verification of the Active Front-End Converters Dynamic Model and Control Designs. *IEEE Transactions on Power Electronics*, April **2011**, vol. 26, no. 4, pp. 1112-1118. **DOI:** 10.1109/TPEL.2010.2097607
15. Fioretto, M.; Raimondo, G.; Rubino, L.; Serbia, N.; Marino, P. Evaluation of current harmonic distortion in wind farm application based on Synchronous Active Front End converters. *AFRICON, 2011*, Livingstone, **2011**, pp. 1-6. **DOI:** 10.1109/AFRCON.2011.6072064

Preprints (www.preprints.org) | NOT PEER-REVIEWED | Posted: 4 September 2018 doi:10.20944/preprints201809.0054.v1

Peer-reviewed version available at *Energies* **2018**, *11*, 2458; doi:10.3390/en11092458

16. Shen, L.; Bozhko, S.; Asher, G.; Patel, C.; Wheeler, P. Active DC-Link Capacitor Harmonic Current Reduction in Two-Level Back-to-Back Converter. *IEEE Transactions on Power Electronics*, Oct. **2016**, vol. 31, no. 10, pp. 6947-6954. **DOI:** 10.1109/TPEL.2015.2511304
17. Cai, X.; Zhang, Z.; Cai, L.; Kennel, R. Current balancing control of high power parallel-connected AFE with small current ripples. *2015 9th International Conference on Power Electronics and ECCE Asia (ICPE-ECCE Asia)*, Seoul, **2015**, pp. 624-630. **DOI:** 10.1109/ICPE.2015.7167849
18. Liu, Ch.; Sun, P.; Lai, J. S.; Ji, Y.; Wang, M.; Chen, C. L.; Cai, G. Cascade dual-boost/buck active-front-end converter for intelligent universal transformer. *IEEE Transactions on Industrial Electronics*, Dec. **2012**, vol. 59, no. 12, pp. 4671-4680. **DOI:** 10.1109/TIE.2011.2182014
19. Hiskens, I.A. Dynamics of Type-3 Wind Turbine Generator Models. *IEEE Transactions on Power Systems*, Feb. **2012**, vol.27, no.1, pp. 465, 474. **DOI:** 10.1109/TPWRS.2011.2161347
20. Yazdani, A.; Iravani, R. Voltage-Sourced Converters in Power Systems: Modeling, Control and Applications. Hoboken, New Jersey, USA: John Wiley & Sons, Inc., 2010, pp. *385-412*. ISBN 978-0-470-52156-4.
21. Orlando, N. A.; Liserre, M.; Mastromauro, R. A.; Dell'Aquila, A. A Survey of Control Issues in PMSG-Based Small Wind-Turbine Systems. *IEEE Transactions on Industrial Informatics*, Aug. **2013**, vol. 9, no. 3, pp. 1211-1221. **DOI:** 10.1109/TII.2013.2272888
22. Salgado-Herrera, N. M.; Medina-Ríos, J. A.; Tapia-Sánchez, R.; Anaya-Lara, O.; Rodríguez-Rodríguez, J. R. DSPWM multilevel technique of 27-levels based on FPGA for the cascaded DC/AC power converter operation. *International Transactions on Electrical Energy Systems*. **2018**; 28:e2479. **https://doi.org/10.1002/etep.2479**

Biographies

Nadia María Salgado-Herrera received the Ph.D. degree in electrical engineering from Universidad Michoacana de San Nicolás de Hidalgo (UMSNH) in 2016, the B.S. and M.S.degrees in electronics engineering and electrical engineering from Instituto Tecnológico de Morelia, Michoacán, México, in 2009 and 2011, respectively. She is currently doing her pos-doctoral research at the University of Strathclyde. Her research interests include power electronics, power quality, and renewable energy.

David Campos-Gaona (Mí12) received the B.E. degree in electronic engineering, and the M.Sc. and Ph.D. degrees in electrical engineering, all from Instituto Tecnolgico de Morelia, Morelia, Mexico, in 2004, 2007, and 2012, respectively. From 2014 to 2016, he was a Postdoctoral Research Fellow with the Department of Electrical and Computer Engineering, University of British Columbia, Vancouver, Canada. Since August 2016 he is with the University of Strathclyde, Glasgow, U.K. where he currently works as a research fellow. His research interest include wind farm power integration, HVDC transmission systems, and real-time digital control of power-electronic-based devices.

Olimpo Anaya-Lara (Mí98) received the B.Eng. and M.Sc. degrees from Instituto TecnolÛgico de Morelia, Morelia, MÈxico, and the Ph.D. degree from the University of Glasgow, Glasgow, U.K., in 1990, 1998, and 2003, respectively. His industrial experience includes periods with Nissan Mexicana, Toluca, Mexico, and CSG Consultants, Coatzacoalcos, MÈxico. Currently, he is a Professor with the Institute for Energy and Environment, University of Strathclyde, Glasgow, U.K. His current research interests include wind generation, power electronics, and stability of mixed generation power systems.

Aurelio Medina-Rios received the Ph.D. degree from the University of Canterbury, Christchurch, New Zealand, in 1992. He has worked as a Post-Doctoral Fellow at the University of Canterbury, New Zealand (1 year) and University of Toronto, Canada (2 years). He is currently a Staff Member in the Facultad de Ingeniería Eléctrica, UMSNH, Morelia, Mexico. His research interests include the dynamic and steady-state analysis of power systems.

Roberto Tapia-Sánchez received the Ph.D. degree from Ecole Centrale de Lille, Lille, France, in 2011. He joined the Faculty of Electrical Engineering, University of Michoacán, Morelia, Mexico, in 2011, where he is currently a

Preprints (www.preprints.org) | NOT PEER-REVIEWED | Posted: 4 September 2018 doi:10.20944/preprints201809.0054.v1

Peer-reviewed version available at *Energies* **2018**, *11*, 2458; doi:10.3390/en11092458

Professor in the Division of Graduate Studies. His research interests include the design and control of renewable energy systems.

Juan R. Rodríguez-Rodríguez received the B.Eng. and Ph.D. degrees in electrical engineering from the Instituto Tecnológico de Morelia, Morelia, Mexico, in 2009 and 2015, respectively. He is currently Associate Professor in the Department of Electrical Energy at UNAM, Mexico. His current research interests include power electronics converters, smart-grids, and renewable energy.